Visualizing Interfacial Collective Reaction Behaviour of Li-S Batteries

Authors: Shiyuan Zhou[1,7], Jie Shi[3,7], Sangui Liu[1], Gen Li[1], Fei Pei[1], Youhu Chen[1], Junxian Deng[1], Qizheng Zheng[1], Jiayi Li,[6] Chen Zhao[2], Inhui Hwang[4], Cheng-Jun Sun[4], Yuzi Liu[5], Yu Deng,[6] Ling Huang[1], Yu Qiao[1], Gui-Liang Xu[2*], Jian-Feng Chen[3], Khalil Amine[2*], Shi-Gang Sun[1] and Hong-Gang Liao[1*]

Affiliations:

[1]State Key Laboratory of Physical Chemistry of Solid Surfaces, Collaborative Innovation Center of Chemistry for Energy Materials, Department of Chemistry, College of Chemistry and Chemical Engineering, Xiamen University, Xiamen 361005, P. R. China

[2]Chemical Sciences and Engineering Division, Argonne National Laboratory, Lemont, IL 60439, USA

[3]State Key Laboratory of Organic Inorganic Composites, Beijing University of Chemical Technology, Beijing 100029, P. R. China

[4]X-ray Science Division, Argonne National Laboratory, Lemont, IL 60439, USA

[5]Centre for Nanoscale Materials, Argonne National Laboratory, Lemont, IL, USA

[6]Department of Materials Science and Engineering, College of Engineering and Applied Sciences, Nanjing University, Nanjing 210093, P. R. China

[7]These authors contributed equally: Shiyuan Zhou, Jie Shi.

*Correspondence to: hgliao@xmu.edu.cn, xug@anl.gov, amine@anl.gov

Abstract

Benefited from high energy density (2600 Wh kg^{-1}) and low cost, lithium-sulfur (Li-S) batteries are considered as promising candidates for advanced energy storage systems[1-4]. Despite tremendous efforts in suppressing the long-standing lithium polysulfides (LiPSs) shuttle effect[5-7], the understanding of interfacial reactions of LiPSs at nanoscale remains elusive. This is mainly due to the limitation of *in situ* characterization tools in tracing liquid/solid conversion of unstable LiPSs at high temporal-spatial resolution[8-10]. The urgent need is to understand the coupled phenomena inside Li-S batteries, specifically, the dynamic distribution, aggregation, deposition, and dissolution of LiPSs. Herein, by using *in situ* liquid-cell electrochemical transmission electron microscopy, we directly visualized the transformation of LiPSs over electrode surfaces at atomic scale. Strikingly, an unexpected gathering-induced collective charge transfer of LiPSs was captured on nanocluster active center immobilized surface. It further induced an instantaneous deposition of nonequilibrium Li_2S nanocrystals from LiPSs dense liquid phase. Without mediation of active centers, the reactions followed a classical single-molecular pathway, LiPSs transforming into Li_2S_2 and Li_2S step by step. Molecular dynamics simulation indicated that the long-range electrostatic interaction between active centers and LiPSs promoted the formation of dense phase consisting of Li^+ and S_n^{2-} ($2<n\leq6$), and the collective charge transfer in dense phase was further verified by *ab initio* molecular dynamics simulation. The collective interfacial reaction pathway unveils a new transformation mechanism and deepens the fundamental understanding for Li-S batteries.

Main

Lithium-sulfur (Li-S) batteries undergo a 16-electron reaction that converts sulfur into a series of lithium polysulfides (LiPSs) with variable chain length. Among them, three-quarters of the capacity is mainly contributed by the reaction from soluble Li_2S_6 to solid Li_2S (Fig. 1a). During this process, the high solubility of LiPSs species and insulating properties of Li_2S_2/Li_2S would lead to continuous loss of active materials and severe capacity degradation[11]. Many strategies have been proposed to increase the energy density and cycling stability, such as structural tailoring of sulfur hosts[12], separators[13], electrolytes[14], etc. However, the fundamental principles underlying these material designs remain poorly understood. For example, what's the rate-limiting step of sluggish reaction kinetics that prevents development of fast-charging Li-S batteries? How does active center keep active to catalyse LiPSs at electrode/electrolyte interfaces?

To study the electrochemical reactions of Li-S batteries, *in situ* characterization techniques, including X-ray diffraction (XRD)[15], X-ray absorption near edge structure (XANES)[16,17], nuclear magnetic resonance (NMR)[18] and Raman spectra[19], are employed. These techniques can provide specific chemical/structural information of reaction intermediates/products; however, they mainly acquire statistical information of mixed signals from both electrolyte and electrode, resulting in the limited understanding of interfacial reaction dynamics of LiPSs. Benefited from the high temporal-spatial resolution, *in situ* transmission electron microscopy (TEM) can track dynamic reactions at atomic/single molecular scale[20,21]. Currently, the open-cell configuration can hardly avoid the spontaneous sublimation of sulfur under high-vacuum environment[22,23], and the previously reported liquid-cell configuration is driven by electron beam (e-beam) instead of electric field[24,25], suffering from the unavoidable susceptibility to beam damage during investigation. The aforementioned *in situ* TEM studies have not yet uncovered the realistic electrochemical redox reactions in liquid electrolytes.

Herein, we constructed a Li-S nanobattery within a liquid cell, and combining with electrochemical TEM (EC-TEM), we achieved high-resolution and real-time observation of LiPSs evolution at electrode surfaces in the ether-based electrolyte (Fig. 1b-d). Our study revealed that active centers gathered soluble LiPSs into a droplet-like dense phase and induced an instantaneous deposition of nonequilibrium nanocrystalline/amorphous Li_2S, rather than a traditional step-by-step transformation. Density functional theory (DFT) calculations and molecular dynamics (MD) simulations pointed out that gathering-induced crystallization was resulted from the long-range electrostatic interaction and collective charge transfer behaviour between active centers and LiPSs droplet-like dense phase.

Configurations of EC-TEM

An electrochemical liquid cell using Ti as electrodes was assembled for Li_2S_6 electrolyte injection, before mounted in an EC-TEM holder (Fig. 1c, Extended Data Fig. 1a-d, and Supplementary Fig. 1). To enhance the spatial resolution in liquid cells, we applied a 100 nm-thick spacer and a ~10 nm SiN_x observation window (more details of instrumental advancements see Supplementary Discussion 1, Extended Data Fig. 1e, f, and Supplementary Figs. 2–4). Cyclic voltammetry (CV) profile acquired in an electrochemical liquid-cell reflected a pair of redox peaks (Fig. 1b), corresponding to the typical liquid-solid transformation of LiPSs. The liquid cell was potentiostatically discharged at –0.5 V for the deposition of Li_2S from soluble Li_2S_n ($Li_2S_n + e^- \rightarrow Li_2S$, $2<n\leq6$). TEM images revealed two distinct forms of deposited Li_2S - ultra-small nanocrystalline (with active centers) and rod-like/plate-like structures (without active centers) - indicating a strong correlation between electrode surfaces and the thermodynamics/kinetics of Li_2S deposition (Fig. 1d).

Single-molecular pathway

High-resolution *in situ* EC-TEM studies were conducted to investigate electrochemical reactions at different electrode surfaces. Since LiPSs intermediates and pure Li_2S were highly susceptible to e-beam damage, all electrochemical processes in liquid cells were conducted with e-beam dose rates below 1.5 e Å^{-2} s^{-1} (more details of e-beam effects see Supplementary Discussion 2 and Supplementary Figs. 5–10). Time-series TEM images and projection area variation revealed the morphology evolution of Li_2S deposition/dissolution without mediation of active centers (Fig. 2a, b and Supplementary Video 1). During potentiostatic discharge at –0.5 V, two types of nucleation-growth pathways were observed: one was a single-step deposition of rod-like/plate-like Li_2S, and the other was a two-step deposition via metastable Li_2S_2. For the two-step pathway, solid nano-nuclei were formed at electrode/electrolyte interface during initial nucleation (marked as particles #1 and #2 in Fig. 2b), which acted as preferred seeds for the subsequent grain growth (25 s). After about 70 s of discharge, the growth rate of primary Li_2S_2 particles slowed down. Then, metastable particle #2 (smaller size) quickly dissolved, while particle #1 (larger size) elongated along its longitudinal orientation (116.2 s). After the complete dissolution of particle #2 and mass redistribution, rod-like Li_2S was formed (137.6 s). During potentiostatic charge (+0.5 V), rod-like Li_2S shortened gradually (201.6 s), and then it decomposed rapidly (219.8 s). The variation in dissolution rate (before/after ~240 s) should be attributed to the insulating property of Li_2S, leading to a large energy barrier at initial stages[26]. Besides, rod-like Li_2S could also be directly deposited through a single-step pathway (Supplementary Fig. 11 and Supplementary Video 2). We also found that the reduced S_n^{2-} ($n \leq 2$) ions were diffusible, resulting in the precipitation of solid Li_2S_n ($n \leq 2$) near the electrode surface (Supplementary Fig. 12).

In situ EC-TEM results indicated that granular Li_2S_2 appeared as a metastable intermediate phase during discharge, making it hard to be captured. By simulating Li_2S_2 candidates with different crystal structures, we found that the tetragonal Li_2S_2 had the lowest formation energy (E_f) compared with that of multiple hexagonal Li_2S_2 (Fig. 2c and Extended Data Fig. 2a-c). The simulated and experimental selected area electron diffraction (SAED) patterns were also highly consistent with the tetragonal Li_2S_2 structure along [001] and [111] directions (Fig. 2d, Extended Data Fig. 2d, e, and Supplementary Fig. 13). The above studies have resolved the controversial structure of Li_2S_2 intermediate from both calculation and experiment[16,27-30]. For rod-like Li_2S, SAED patterns indicated the [111], [011], and [100] directions of face-center-cubic (FCC) structure (Fig. 2e and Extended Data Fig. 2f). High-angle annular dark field scanning TEM (HAADF-STEM) image and linear element distributions of energy dispersive X-ray spectrometry (EDS) confirmed the uniform S distribution in the rod-like structure (Fig. 2f and Extended Data Fig. 2g).

We investigated various electrolyte concentrations and discharge potentials to understand the mechanism behind different deposition pathways. Our results indicated that increasing the concentration of Li_2S_6 electrolyte (20 and 50 mM) did not affect the nucleation-growth pathway (Supplementary Fig. 14). However, changing the discharge potential resulted in distinct outcomes. At –0.5 V, granular and rod-like structures formed simultaneously (Supplementary Fig. 15), while at –0.1 V, solid discharge products primarily nucleated in granular structures, which transformed into rod-like/plate-like Li_2S as the deposition progressed (Extended Data Fig. 3 and Supplementary Video 3). The reaction at –0.1 V corresponds to a typical two-step deposition, which is also the main pathway of Li_2S deposition without active centers. According to the Lifshitz-Slyozov-Wagner model (LSW, Area $\propto t^n$), the initial deposition at both –0.1 and –0.5 V followed a reaction-limited stage[31-33] (Supplementary Fig. 16). This indicated that Li_2S deposition was predominantly controlled by the charge transfer at the electrode surface (Supplementary Fig. 17).

Collective pathway

To investigate the effect of metallic active centers in LiPSs redox reactions, Mo nanoclusters/N-doped graphene (Mo NCs/N-G) was rationally designed (more details of structure characterization of Mo NCs/N-G see Methods, Fig. 3a-c, and Supplementary Figs. 18–20). During potentiostatic discharge at −0.5 V (Fig. 3d and Supplementary Video 4), no nucleation-growth of rod-like Li_2S was observed (Extended Data Fig. 4a, 65/125 s), while Mo NCs/N-G nanosheet gradually spread out instead (185 s). Subsequent observation under a higher resolution revealed that many dark areas formed on the edge and surface of graphene during discharge (Extended Data Fig. 4b, and Supplementary Video 5), corresponding to Li_2S deposition on Mo NCs/N-G nanosheet. Such a preferential reactivity of active centers was further confirmed in a higher concentration electrolyte (100 mM Li_2S_6, Supplementary Video 6). Compared with bare electrode surface and Mo NCs/N-G nanosheet located at bottom left without electronic contact, a distinct contrast variation was observed due to the Li_2S deposition on Mo NCs/N-G nanosheet that was in direct contact with Ti electrode (highlighted by red frame in Extended Data Fig. 4c).

The structure of Li_2S was investigated at atomic-scale after the electrochemical deposition on Mo NCs/N-G nanosheet in liquid cells (more details see Supplementary Discussion 3, Extended Data Fig. 5, and Supplementary Fig. 21). High-resolution transmission electron microscopy (HRTEM) image revealed that Li_2S was deposited in a nonequilibrium crystal form on Mo NCs/N-G nanosheet (Fig. 3e). The deposited areas were composed of both nanocrystalline and amorphous Li_2S (Fig. 3f and Supplementary Fig. 22), in contrast to the single-crystalline FCC Li_2S deposited on bare electrode surface. The spatial distribution of crystallized Li_2S domains was extracted by the inversed fast Fourier transform (FFT) frequencies of HRTEM image (Fig. 3g and Supplementary Fig. 23), which revealed the randomly exposed crystal planes of Li_2S nanocrystalline. It was further confirmed by the poly-crystalline diffraction rings of SAED pattern (Fig. 3h). By comparing crystal structures between HRTEM images and simulated images (Fig. 3i and Supplementary Figs. 24 and 25), we could index the zone axis of FCC Li_2S nanocrystalline mainly along [111], [100], and [011] directions (more details of image acquiring and processing see Supplementary Discussion 4).

The interfacial reactions and reversibility of LiPSs mediated by active centers were further investigated under potentiostatic conditions at ±0.5 V (Fig. 4a). Multiple droplet-like structures were formed during the first discharge at –0.5 V, and Li_2S deposition at active center-mediated surface underwent gathering, conversion, and crystallization (marked as droplets #1, #2, and #3, Fig. 4b, Extended Data Fig. 6a, and Supplementary Video 7). Typically, for liquid droplet #1 (Extended Data Fig. 6b), it underwent continuous gathering and growth (40 s to 45.2 s). Subsequently, the droplet moved vigorously as it grew further (53.4 s to 59.2 s), but remained anchored on active center due to the strong binding affinity towards LiPSs, rather than diffusing into electrolyte. According to the LSW model (Fig. 4a and Extended Data Fig. 6c), the gathering of liquid droplets #1, #2, and #3 followed a reaction-limited process, indicating that the charge transfer was the rate-limiting step. After that, rapid deposition of Li_2S from LiPSs droplets occurred within five seconds, a similar spreading and edge-roughening of Mo NCs/N-G nanosheet was observed (Extended Data Fig. 6c). During redox reactions, the surface of Mo NCs/N-G was observed to periodically get clear and blurry (239.2 s and 319.4 s, Fig. 4b), corresponding to the reversible solid-liquid phase transformation of LiPSs mediated by active centers.

The droplet-like structures were analyzed. The irregular and ever-changing edges, along with low contrast, indicate that these structures are not crystallized or nucleated Li_2S_2/Li_2S but highly concentrated Li_2S_n ($2<n\leq6$) gathered by active centers. According to literatures, a dense liquid phase could form through a liquid-liquid phase segregation, triggered by concentration difference[34,35]. This phenomenon is thermodynamically favourable and can considerably reduce the surface free energy relative to the solution-crystal interfaces[36,37]. HRTEM images along with their FFT and SAED patterns revealed the structures of droplet-like dense phase and Li_2S nanoparticles (Extended Data Fig. 7a, b), while HAADF-STEM images and EDS mappings confirmed a high concentration of sulfur in the dense phase. In electron energy loss spectra (EELS, Fig. 4c), the sulfur $L_{2,3}$ and L_1 edge peaks should be located at 162–185 eV and 238 eV respectively[23,24]. These peaks were absent in the bulk electrolyte, but were found in the dense phase with two peaks at 173.5 eV and 180.7 eV. The sulfur-L edge peaks in Li_2S nanocrystalline were significantly stronger and showed a chemical redshift compared with the dense phase, which should be attributed to the electrochemical reduction from S_n^{2-} ($2<n\leq6$) to S^{2-}. The formation of multiple droplets on the surface of Mo NCs/N-G nanosheets was further confirmed by HRTEM

images and Z-contrast analysis of HAADF-STEM images (Extended Data Fig. 7c-f and Supplementary Figs. 26 and 27).

Interaction of active centers with LiPSs was commonly attributed to the chemical bonding[2,3]. However, the interaction could be more complex at the nano/micro scale, likely involving electrostatic force, van der Waals force, and surface molecular force[38,39]. To quantitatively analysis the interfacial reaction of LiPSs dense phase, we tracked the centroid motion of droplet #1 and used the Einstein-Stokes equation to calculate the interaction force (F, pN) and velocity (v, nm s^{-1}) of droplet #1 towards active centers over time (Fig. 4d and Extended Data Fig. 6b, d). Our results revealed that the strong interaction between active centers and LiPSs stabilized the droplet-like dense phase during initial gathering (overlapped in red). Subsequently, droplet #1 experienced a continuous waggle on the surface, which should be ascribed to the simultaneous gathering and electrochemical reduction of S_n^{2-} ($2<n\leq6$, overlapped in red-blue gradient). Finally, the drift velocity decreased gradually before reaching the threshold for instantaneous crystallization. *In situ* observation revealed that droplet-like dense phase was grabbed by active centers, and the size could reach a diameter of ~30 nm, indicating a long-range and strong interaction.

Simulations and calculations

To understand the formation and transformation mechanism of droplet-like dense phase, we established MD models to study the reaction dynamics of LiPSs. Comparing the electrode surfaces of Mo NCs/N-G and Ti, our simulations revealed that Mo active centers were able to attract S_6^{2-} from the bulk solution, independent of electrolyte concentration (Extended Data Fig. 8a-c, Supplementary Figs. 28–30, and Supplementary Video 8). Statistical analysis indicated a stronger long-range attraction towards S_6^{2-} ions of Mo active centers than the Ti surface (Extended Data Fig. 8d). MD simulation and Z-axis position analysis revealed that the dense phase composed of S_6^{2-} and Li^+ ion-complex continuously approached to Mo NCs/N-G surface (Fig. 4e, Extended Data Fig. 8e, and Supplementary Video 9). In contrast, Ti surface showed no interaction to LiPSs (Supplementary Fig. 31a and Supplementary Video 10), despite DFT calculations indicating that Ti (001) had a higher adsorption energy towards Li_2S_n than Mo active centers (Supplementary Fig. 31b). This suggests that Ti surface can only provide the strong chemical bonding but poor long-range interaction towards LiPSs. By analyzing mean square displacement (MSD) curves along the Z-axis (Extended Data Fig. 8f), we found that the diffusion coefficient of droplet-like dense phase at Mo NCs/N-G surface was enhanced by two orders of magnitude compared with that of Ti surface. DFT calculations revealed that the charge of metallic Mo center was +7.37 e (Supplementary Fig. 31c). Therefore, the strong interaction between Mo active centers and LiPSs droplet should be attributed to electrostatic force. Analysis of the charge of S_6^{2-} ions in the dense ion-complex phase revealed a dynamic variation over time and became more concentrated from bulk to surface along Z-axis (Fig. 4f and Supplementary Fig. 31d). The charge transfer between Mo active centers and Li_2S_6 was investigated by *ab initio* molecular dynamics (AIMD) simulations. By comparing the charge distribution of multiple Li_2S_6 molecules in the dense phase before and after applying an electrode potential, we found that electrons were transferred and shared from Mo active centers to polysulfide ions in the dense phase, from internal to external layers, rather than only the Li_2S_6 molecules close to the active centers (Extended Data Fig. 8g, more details of simulations see Supplementary Discussion 5). The investigations confirm that the long-range gathering effect of Mo active centers induces the formation of droplet-like dense phases, and then these droplets work as integral reaction units, allowing charge transfer among S_6^{2-} ions.

Electrochemical investigations

To validate LiPSs reactions over different surfaces, we conducted parallel investigation on the discharge products in coin-type cells, the gathering of soluble LiPSs and their fast conversion into solid Li_2S were confirmed by *ex situ* characterizations (more details see Supplementary Discussion 6 and Supplementary Figs. 32–34). Potentiostatic discharge coin-type cells showed faster reaction kinetics and higher Li_2S deposition capacity with the mediation of active centers (Extended Data Fig. 9a), which were 1410 s ahead of peak current and 2.4 times higher in capacity. Electrochemical impedance spectroscopy (EIS) revealed a much smaller charge transfer resistance after Li_2S deposition (6.9 ohm versus 132.7 ohm, Extended Data Fig. 9b and Supplementary Fig. 35a) and higher reversibility in the subsequent Li_2S dissolution with active centers (Extended Data Fig. 9c). The activation energy (E_a) was significantly reduced during the liquid-solid transformation of LiPSs (Extended Data Fig. 9d, e and Supplementary Fig. 36). In symmetric cells (Extended Data Fig. 9f and Supplementary Fig. 35b), Mo NCs/N-G demonstrated a smaller potential gap of the redox peaks (0.67 V versus 0.82 V) and ten times higher current density. Galvanostatic tests of Mo NCs/N-G and Ti electrode showed a 2.07 times higher capacity retention rate with active centers (Extended Data Fig. 9g). Specifically, the initial redox reaction of LiPSs revealed a much lower nucleation/dissolution barrier and voltage polarization, and the potential barrier of Li_2S dissolution almost vanished starting from the 2nd cycle (Extended Data Fig. 9h, i). Furthermore, the application potential of Mo active centers in Li-S full cells was demonstrated under realistic working conditions, including high mass loading, fast charging, and lean electrolyte conditions (more details of electrochemical performance see Methods, Extended Data Fig. 10).

Discussion

During multi-electron reactions of Li-S batteries, the adsorption, catalysis, and conversion between LiPSs intermediates and active centers are involved, and the complexity of reaction kinetics governing Li_2S deposition/dissolution leads to the diverse and ambiguous pathways. In this work, by using high temporal-spatial resolution *in situ* EC-TEM, we revealed that active centers gathered soluble LiPSs into droplet-like dense phase and thus induced an instantaneous crystallization, rather than a classical step-by-step transformation. Besides, our preliminary results suggest that the collective reaction mechanism seems to be universal to other metal active centers, which needs more systematic investigations. Previous studies of material/surface modification mainly focused on clarifying the adsorption and catalysis mechanism from single-molecular aspect. Our experiment and simulation results indicated that the aggregation state and collective behaviour of ions and molecules played a critical role in the kinetics of electrochemical interfacial reactions. The collective mechanism provides new insight into constructing next-generation high-energy, long-life, and fast-charging Li-S batteries.

Reference

1. Ji, X., Lee, K. T. & Nazar, L. F. A highly ordered nanostructured carbon-sulphur cathode for lithium-sulphur batteries. *Nat. Mater.* **8**, 500-506 (2009).
2. Zhao, C. *et al.* A high-energy and long-cycling lithium-sulfur pouch cell via a macroporous catalytic cathode with double-end binding sites. *Nat. Nanotechnol.* **16**, 166-173 (2021).
3. Peng, L. *et al.* A fundamental look at electrocatalytic sulfur reduction reaction. *Nat. Catal.* **3**, 762-770 (2020).
4. Shen, Z. *et al.* Cation-doped ZnS catalysts for polysulfide conversion in lithium–sulfur batteries. *Nat. Catal.* **5**, 555-563 (2022).
5. Chen, H. *et al.* Catalytic materials for lithium-sulfur batteries: mechanisms, design strategies and future perspective. *Mater. Today* **52**, 364-388 (2021).
6. Liu, Y. *et al.* Electrolyte solutions design for lithium-sulfur batteries. *Joule* **5**, 2323-2364 (2021).
7. Liang, Z. *et al.* Advances in the Development of Single-Atom Catalysts for High-Energy-Density Lithium-Sulfur Batteries. *Adv. Mater.* e2200102 (2022).
8. Rehman, S., Pope, M., Tao, S. & McCalla, E. Evaluating the effectiveness of in situ characterization techniques in overcoming mechanistic limitations in lithium–sulfur batteries. *Energy Environ. Sci.* **15**, 1423-1460 (2022).
9. Ross, F. M. Opportunities and challenges in liquid cell electron microscopy. *Science* **350**, aaa9886 (2015).
10. Zeng, C. *et al.* Dynamic investigation of battery materials via advanced visualization: from particle, electrode to cell level. *Adv. Mater.* **34**, e2200777 (2022).

11. Kong, L. *et al.* Current-density dependence of Li_2S/Li_2S_2 growth in lithium–sulfur batteries. *Energy Environ. Sci.* **12**, 2976-2982 (2019).
12. X., Z. G., H., Z. A. W. & L., Z. F. Nitrogen-sulfur co-doped porous carbon preparation and its application in lithium-sulfur batteries. *J. Electrochem.* **27**, 614-623 (2021).
13. Pei, F. *et al.* A Two-Dimensional Porous Carbon-Modified Separator for High-Energy-Density Li-S Batteries. *Joule* **2**, 323-336 (2018).
14. Tsao, Y. *et al.* Designing a Quinone-Based Redox Mediator to Facilitate Li_2S Oxidation in Li-S Batteries. *Joule* **3**, 872-884 (2019).
15. Nelson, J. *et al.* In Operando X-ray diffraction and transmission X-ray microscopy of lithium sulfur batteries. *J. Am. Chem. Soc.* **134**, 6337-6343 (2012).
16. Cuisinier, M. *et al.* Sulfur Speciation in Li–S Batteries Determined by Operando X-ray Absorption Spectroscopy. *J. Phys. Chem. Lett.* **4**, 3227-3232 (2013).
17. Li, M. *et al.* Evidence of Morphological Change in Sulfur Cathodes upon Irradiation by Synchrotron X-rays. *ACS Energy Lett.* **7**, 577-582 (2022).
18. See, K. A. *et al.* Ab initio structure search and in situ 7Li NMR studies of discharge products in the Li-S battery system. *J. Am. Chem. Soc.* **136**, 16368-16377 (2014).
19. Chen, J.-J. *et al.* Conductive Lewis Base Matrix to Recover the Missing Link of Li_2S_8 during the Sulfur Redox Cycle in Li–S Battery. *Chem. Mater.* **27**, 2048-2055 (2015).
20. Sun, X. *et al.* Dislocation-induced stop-and-go kinetics of interfacial transformations. *Nature* **607**, 708-713 (2022).
21. Frey, H. *et al.* Dynamic interplay between metal nanoparticles and oxide support under redox conditions. *Science*, 982–987 (2022).
22. Kim, H. *et al.* In Situ TEM Observation of Electrochemical Lithiation of Sulfur Confined within Inner Cylindrical Pores of Carbon Nanotubes. *Adv. Energy Mater.* **5** 1501306 (2015).
23. Wang, Z. *et al.* In Situ TEM Observations of Discharging/Charging of Solid-State Lithium-Sulfur Batteries at High Temperatures. *Small* **16**, 2001899 (2020).
24. Xu, Z.-L. *et al.* Visualization of regulated nucleation and growth of lithium sulfides for high energy lithium sulfur batteries. *Energy Environ. Sci.* **12**, 3144-3155 (2019).
25. Seo, H. K. *et al.* Direct Visualization of Lithium Polysulfides and Their Suppression in Liquid Electrolyte. *Nano Lett.* **20**, 2080-2086 (2020).
26. Zhang, L. *et al.* Revealing the Electrochemical Charging Mechanism of Nanosized Li_2S by in Situ and Operando X-ray Absorption Spectroscopy. *Nano Lett.* **17**, 5084-5091 (2017).
27. Conder, J. *et al.* Direct observation of lithium polysulfides in lithium–sulfur batteries using operando X-ray diffraction. *Nat. Energy* **2**, 17069 (2017).
28. Yang, G., Shi, S., Yang, J. & Ma, Y. Insight into the role of Li_2S_2 in Li–S batteries: a first-principles study. *J. Mater. Chem. A* **3**, 8865-8869 (2015).
29. Feng, Z. *et al.* Unravelling the role of Li_2S_2 in lithium–sulfur batteries: A first principles study of its energetic and electronic properties. *J. Power Sources* **272**, 518-521 (2014).
30. Paolella, A. *et al.* Transient existence of crystalline lithium disulfide Li_2S_2 in a lithium-sulfur battery. *J. Power Sources* **325**, 641-645 (2016).
31. Wagner, C. Theory of precipitate change by redissolution. *Z. Elektrochem.* **65**, 581-591 (1961).
32. Lifshitz, I. M. & Slyozov, V. V. The kinetics of precipitation from supersaturated solid solutions. *J. Phys. Chem. Solids* **19**, 35-50 (1961).
33. Viswanatha, R. & Sarma, D. D. in *Nanomaterials Chemistry* 139-170 (2007).
34. Gower, L. B. & Odom, D. J. Deposition of calcium carbonate films by a polymer-induced liquid-precursor (PILP) process. *J. Cryst. Growth* **210**, 719-734 (2000).
35. Smeets, P. J. *et al.* Calcium carbonate nucleation driven by ion binding in a biomimetic matrix revealed by in situ electron microscopy. *Nat. Mater.* **14**, 394-399 (2015).
36. Wallace, A. F. *et al.* Microscopic Evidence for Liquid-Liquid Separation in Supersaturated $CaCO_3$ Solutions. *Science* **341**, 885-889 (2013).
37. De Yoreo, J. J. *et al.* Crystallization by particle attachment in synthetic, biogenic, and geologic environments. *Science* **349**, aaa6760 (2015).
38. Min, Y. J. *et al.* The role of interparticle and external forces in nanoparticle assembly. *Nat. Mater.* **7**, 527-538 (2008).
39. Bishop, K. J., Wilmer, C. E., Soh, S. & Grzybowski, B. A. Nanoscale forces and their uses in self-assembly. *Small* **5**, 1600-1630 (2009).

Figure Legends

Fig. 1 | Design of liquid-cell EC-TEM to investigate LiPSs interfacial reactions. (a) Comparison of charge/discharge profiles of desirable and undesirable Li_2S_6–Li_2S reactions in Li-S batteries. (b) CV profile obtained in an electrochemical liquid cell at a scan rate of 10 mV s^{-1} showing the reduction of Li_2S_6 and oxidation of Li_2S. (c) Configuration of liquid-cell EC-TEM and schematic illustration of electrochemical reactions of LiPSs at different electrode/electrolyte interfaces. WE = working electrode, CE/RE = counter/reference electrodes. (d) Typical (HR)TEM images of deposited Li_2S at different electrode surfaces (with/without active centers) after potentiostatic discharge at –0.5 V for 300 s in an electrochemical liquid cell. 10 mM Li_2S_6 was used as the electrolyte.

Fig. 2 | Interfacial reactions and structures of LiPSs without mediation of active centers. (a) The applied electric field and the corresponding projection area variation as a function of time of particles #1 and #2. The electrochemical liquid cell was first potentiostatically discharged at –0.5 V, and then potentiostatically charged at +0.5 V for 150 s, respectively. 10 mM Li_2S_6 was used as the electrolyte. Error bars represent standard deviations of the measurement. (b) Time-series TEM images from Supplementary Video 1 of Li_2S deposition (red frame) and dissolution (blue frame) in an electrochemical liquid cell. The white and orange arrows indicate the directions of charge transfer and LiPSs diffusion, respectively. (c) The energy comparison between tetragonal P42/mnm Li_2S_2 and hexagonal P$\bar{6}$2m and P63/mmc Li_2S_2. The inset is the crystal structure of tetragonal Li_2S_2 unit cell with the lowest E_f, where Li and S atoms are represented by red and blue balls. (d) SAED pattern of granular Li_2S_2 (tetragonal, $P4_2/mnm$) along [001] direction. (e) SAED pattern of rod-like Li_2S (cubic, Fm-3m) along [111] direction. (f) EDS spectrum, STEM image, and S element mapping of Li_2S. The corresponding TEM images of the SAED patterns of Li_2S_2 and Li_2S are provided in Supplementary Fig. 13.

Fig. 3 | Structure of deposited Li_2S with mediation of active centers. (a, b) HRTEM and STEM images of Mo NCs/N-G showing the isolated Mo nanoclusters. (c) Fourier transform of extended X-ray absorption fine structure (FT-EXAFS) in R space for Mo NCs/N-G and reference samples of Mo foil, MoO_2, and MoO_3. (d) The applied electric field to the observing area with potentiostatic discharge at –0.5 V. The inset TEM image was from Supplementary Video 4 using 10 mM Li_2S_6 as the electrolyte. (e, f) HRTEM images of deposited Li_2S on Mo NCs/N-G after potentiostatic discharge at –0.5 V in an electrochemical liquid cell. Insets are the corresponding FFT patterns showing the amorphous and crystallized Li_2S at different areas. (g) An inversed FFT patterns from HRTEM image in Supplementary Fig. 23, showing that Li_2S nanocrystalline was mainly composed of (111), (200), and (220) crystal planes, overlapped in red, blue, and green colours, respectively. (h) SAED pattern and the corresponding intensity integration, showing the diffraction peaks of poly-crystalline Li_2S. Q is the scattering vector calculated by $2\pi/d$, where d is the layer spacing. (i) Radial Weiner filtered HRTEM images and FFT patterns of deposited Li_2S

nanocrystalline along [111], [100], and [011] directions. The corresponding simulated HRTEM images and models of Li_2S supercell are presented alongside. Raw HRTEM images are provided in Supplementary Figs. 24 and 25.

Fig. 4 | Interfacial redox reactions of LiPSs with mediation of active centers. (a) The applied electric field and the corresponding projection area variation as a function of time of droplet #1 in Fig. 4b. The liquid cell underwent potentiostatic discharge/charge at ±0.5 V with 120 s for each step. 10 mM Li_2S_6 was used as the electrolyte. A power function was used to fit the area variation over time (Area $\propto t^n$) according to LSW model, where $n \geqslant 1$ represents reaction-limited growth. Error bars represent standard deviations of the measurement. (b) Time-series TEM images from Supplementary Video 7 showing the consecutive potentiostatic discharge/charge with mediation of active centers. (c) EELS of the sulfur-L edge peaks of blank LiPSs electrolyte, droplet-like dense phase (area I, Extended Data Fig. 7a), and Li_2S nanocrystalline (area II, Extended Data Fig. 7b). (d) Variation of interaction force and velocity of droplet #1. The overlapped areas in red and red-blue gradient colours are based on error bars showing the standard deviation. The display point is selected every three data. (e) Time-series MD simulations showing the gathering of LiPSs by Mo active centers into dense ion-complex phase consisting of Li^+ and S_6^{2-} with Li_2S_6 concentration of 17.93 wt%. DFT calculated the charge quantity of Mo active centers (Q = +7.37 e). Z-axis distance between Mo active centers and dense ion-complex phase decreased continuously during the simulation from 42 to 82 ns. The corresponding statistics are provided in Extended Data Fig. 8e. (f) The charge density variation of S_6^{2-} ions along Z-axis as a function of time. The charge distribution of S_6^{2-} ions in dense ion-complex phase was continuously enhanced from bulk to surface. (g) Schematic illustration of interfacial reactions mediated by active centers, showing a gathering-induced collective charge transfer for Li_2S deposition.

Methods

Sample synthesis

Synthesis of $(NH_4)_{42}[Mo^{VI}_{72}Mo^{V}_{60}O_{372}(CH_3COO)_{30}\cdot(H_2O)_{72}]$ polyoxometalates (Mo_{132} POMs). $(NH_4)_{42}[Mo^{VI}_{72}Mo^{V}_{60}O_{372}(CH_3COO)_{30}\cdot(H_2O)_{72}]$ was synthesized following the reported method[40]. Specifically, 4.5 mmol $(NH_4)_6Mo_7O_{24}\cdot 4H_2O$ and 162.2 mmol CH_3COONH_4 was dissolved in 250 mL deionized water under stirring. 6.1 mmol $N_2H_6\cdot SO_4$ was add to the above solution followed by further stirring for 10 min. Then, 83 mL CH_3COOH (50%, v/v) was added. The obtained solution was transferred to an Erlenmeyer flask and left to stand at 20°C for 4 days. The product was washed by ethanol and diethyl ether for several times, followed by subsequent drying to obtain reddish-brown crystals.

Synthesis of ethylenediamine-functionalized reduced graphene oxide (EDA-rGO). GO was chemically exfoliated from graphite according to the modified Hummers method[41]. First, the nucleophilic ring-opening reaction of epoxy groups was used to immobilize the amino group on it, and at the same time, rGO was obtained due to the removal of oxygen-containing groups. Specifically, 60 mg GO nanosheets was uniformly dispersed in 60 mL deionized water, and 120 μL EDA was added under vigorous stirring. The homogeneous solution was transferred into a Teflon-lined stainless-steel autoclave, heating at 75°C for 6 h. After cooling to room temperature naturally, the product was washed by deionized water for several times followed by subsequent freeze-drying, and EDA-rGO was obtained.

Synthesis of Mo NCs/N-G and N-G. Mo NCs/N-G was mainly prepared by the electrostatic interaction between negatively charged Mo_{132} POMs and positively charged EDA-rGO (protonated), which were strongly coupled to form the Mo_{132} POMs/EDA-rGO. The steric confinement and monomolecular dispersion properties of POMs in the Mo_{132} POMs/EDA-rGO composite favoured the formation of atomically dispersed active sites during thermal annealing. Specifically, 30 mg EDA-rGO was ultrasonically dispersed in 30 mL deionized water for 0.5 h followed by vigorous stirring. Then, the pH value of EDA-rGO solution was adjusted to 4.0 with the addition of 120 μL 1 M HCl solution. Meanwhile, 3 mg Mo_{132} POMs were uniformly dispersed in 30 mL deionized water and dropwise added into EDA-rGO solution. After continuous stirring for 12 h, the product was washed by deionized water for several times followed by subsequent freeze-drying, and Mo_{132} POMs/EDA-rGO was obtained. Mo_{132} POMs/EDA-rGO was annealed at 750°C for 1 h under Ar atmosphere with a heating rate of 10°C min^{-1}, and Mo NCs/N-G was finally obtained.

Synthesis of Mo NCs/N-G/S. Mo NCs/N-G/S was prepared through a sulfur melt-diffusing process. Specifically, Mo NCs/N-G was mixed with sulfur at the weight ratio of 1:4 by sufficient grinding. The homogeneous mixture was heated at 155°C under Ar atmosphere for 12 h. After natural cooling to room temperature, it was taken out and ground, followed by reheating under the same conditions to uniformly composite with sulfur.

Structure characterization

The morphology and element distribution of Mo NCs/N-G was characterized by FEI Talos F200S equipped with a Super-X EDS system, and FEI Themis Z G2 30–300 with both image and probe correctors. Dual-EELS were acquired for the electrolyte, droplet-like dense phase, and Li_2S nanocrystalline in electrochemical liquid cells using a Titan G2 (S)TEM operated at 60–300 kV with an energy resolution of 0.8 eV. The raw EELS were processed by background removement (power law) and plural scattering removement (Fourier-ratio). The chemical environment and bonding information were detected by X-ray photoelectron spectroscopy (XPS, PHOIBOS150, Germany). The powder crystalline structure of Mo NCs/N-G and Li_2S deposited electrodes was investigated by XRD with Cu-Kα radiation (Bruker D8 A25, Germany, λ = 1.5418 Å). X-ray absorption fine-structure spectra at the Mo K edge were acquired by a Si (111) monochromator at beamline 20-BM of the Advanced Photon Source. The beamline energy resolution was about $\Delta E/E = 1.3 \times 10^{-4}$. X-ray absorption spectroscopy data was processed using Athena and Artemis software packages. The weight ratio of metallic Mo nanoclusters was measured by Inductively Coupled Plasma Optical Emission Spectrometer (ICP-OES, Agilent, 720ES, USA). After the disassembly of the coin-type cells in an argon-filled glovebox and transferring into tailor-made device to prevent air pollution, *ex situ* characterizations were conducted. Laser confocal Raman spectra were collected on a Nanophoton spectrometer (Laser source: 532 nm, 600 gr mm^{-1}, ND = 180, Exposure time = 5 s). The optical absorbance spectra were analyzed by Ultraviolet-visible spectroscopy (UV-Vis, Shimadzu UV-3600). The morphology was characterized by field emission scanning electron microscope (SEM, ZEISS, Germany).

In situ liquid-cell EC-TEM experiment setup and observation

In situ EC-TEM holder was purchased from Chip-Nova (Xiamen, China), and liquid cells were customized made. Two silicon wafers were used as bottom and top chips, on which an observation window of 10 nm-thick low-stress SiN_x membrane was constructed. Ti WE and CE/RE were deposited on the bottom chip with a face-to-face distance of 200 μm. Before the assembly of bottom and top chips, Mo NCs/N-G was transferred onto the Ti electrodes of bottom chip. The bare chips were also assembled to study LiPSs transformation without mediation of active centers. Electrolyte was prepared by mixing 10/20/50/100 mM Li_2S_6 (S and Li_2S, molar ration: 5:1) in 1 M lithium bis(trifluoromethanesulphonyl)imide (LiTFSI) in 1,3-dioxolane (DOL)/1,2-dimethoxyethane (DME) (v/v = 1:1) electrolyte, followed by stirring overnight. The entire processes of electrolyte injection and chip sealing were performed in the Ar-filled glovebox (H_2O<0.01 ppm, O_2<0.01 ppm). Ether-based electrolyte was added into a reservoir using a syringe, which would flow into the observation window by capillary force, and then epoxy was used to seal the liquid cell. The sealed liquid cell needed to stand for 12 h to stabilize the internal solution environment. Then, the liquid cell was placed into a custom-made EC-TEM holder and applying an electric field by an electrochemical workstation (CHI 660E). *In situ* EC-TEM experiment was performed in a FEI Talos with an acceleration voltage of 200 kV. To avoid the influence of e-beam effect, the e-beam dose rate was controlled below 1.5 e^{-} Å^{-2} s^{-1} for *in situ* electrochemical experiments. Multislice simulation was conducted to simulate HRTEM images of Li_2S nanocrystalline acquired in an electrochemical liquid cell[42,43]. A self-written MATLAB script was used to build the crystal models of Li_2S along [111], [100], and [011] directions. HRTEM images were simulated based on the following parameters: accelerating voltage (200 kV), spherical aberration coefficient (C_s = 1.2 mm), chromatic aberration coefficient (C_c = 1.5 mm), sample thickness (around 5 nm), and defocus (Δf = 40 nm).

Electrochemical measurements

Potentiostatic deposition and dissolution of Li_2S. 100 mM Li_2S_6 prepared as above was used as the electrolyte for Li_2S potentiostatic nucleation. Slurry was prepared by ball milling the mixture of 80 wt% sulfur-free electrode material (Mo NCs/N-G) and 20 wt% LA133 aqueous binder, which was then coated on Ti mesh disks (16 mm in diameter). The areal loading of active material was controlled at around 0.5 mg cm^{-2}. For cell assembly, 20 µL 100 mM Li_2S_6 electrolyte was added to the cathode side, and 20 µL of regular electrolyte (1 M LiTFSI in 1:1 (v/v) DOL/DME) was added to the Li anode side. The assembled cells were galvanostatically discharged to 2.06 V at 0.112 mA and then kept potentiostatically at 2.05 V for the nucleation and growth of Li_2S until the current was below 0.01 mA. For Li_2S dissolution, the cells were further galvanostatically discharged to 1.8 V at 0.01 mA and then kept potentiostatically at 2.4 V until the current was below 0.01 mA. The capacity of deposited Li_2S was calculated according to Faraday's law.

Activation energy. The coin-type cells were galvanostatically discharged to specific discharge potentials at 16 µA cm^{-2} with 100 mM Li_2S_6 electrolyte. The cells were held at the same potential, using chronoamperometry, until a stable output current was achieved. EIS was tested at the frequency range from 100 kHz to 10 mHz from 2.0 to 1.7 V using Multi Autolab electrochemical workstation (M204, Netherlands).

Symmetry cells. CV symmetric cells, both with and without active centers, were collected and compared at a scan rate of 0.1 mV s^{-1}, ranging from −1.0 to 1.0 V. The electrodes decorated with Mo NCs/N-G nanosheets were further tested at increasing scan rates from 0.1 to 1 mV s^{-1}.

Li-S batteries. The slurry was prepared by ball milling the mixture of 80 wt% electrode material (Mo NCs/N-G/S), 10 wt% acetylene black, and 10 wt% LA133 aqueous binder (15 wt%, aqueous dispersion of acrylonitrile copolymer). The uniform slurry was coated on aluminium foil, drying at 60°C for 10 hours in vacuum. The cathode was cut into disc with an areal loading of 1.13 cm^2 (12 mm in diameter). The sulfur areal loading was controlled at around 2 mg cm^{-2} for cycling performance at 1/2/3 C and rate performance. For high sulfur loading test at 0.2 C, the slurry was coated on the self-standing carbon-nanofiber-based electrode prepared by electrospinning, with sulfur areal loading of 2, 3.5, 5.4, and 7 mg cm^{-2}. The electrolyte is about 17.7 (2 mg cm^{-2}) and 10.1 (3.5 mg cm^{-2}) µl mg^{-1}_{S} for regular cells, and 4.3 (5.4 mg cm^{-2}) and 5.1 (7 mg cm^{-2}) for high-loading cells. Coin-type cells were used for electrochemical performance (CR2032). Mo NCs/N-G/S cathode was assembled with Li anode, ether-based electrolyte and polypropylene separators (Celgard 2325) in an argon-filled glovebox. 1 M LiTFSI in 1:1 (v/v) DOL/DME with 2 wt% $LiNO_3$ was used as the electrolyte. The electrochemical tests were carried out on a Neware battery cycler (CT-4008T-5V20mA-164, Shenzhen, China) with a voltage window of 1.8–2.8 V versus Li/Li^+. All electrochemical tests were carried out at room temperature.

Interaction force between active centers and droplet-like dense phase

The MSD of a randomly diffusing molecular is proportional to its diffusing time (MSD = nDt). D is the diffusion coefficient. For *in situ* EC-TEM study in a liquid cell, the molecular diffusion is considered in a two-dimensional space (three-dimensional space n = 6, two-dimensional space n = 4), so the MSD relation gives[44,45]:

$$\mathrm{MSD} = 4Dt \quad \text{(Eq. S1)}$$

The diffusion coefficient of droplet-like dense phase was estimated by tracking its centroid movement in Fig. 4b. The two-dimensional moving trajectory and edge variation profile were shown in Extended Data Fig. 6b. According to the MSD as a function of time (Eq. S1 and Extended Data Fig. 6d), the diffusion coefficient ($D = 4.71\ nm^2\ s^{-1}$) of droplet #1 was obtained by a linear fit, which was similar to other reported *in situ* TEM studies of Li-S batteries[32,34]. The difference of diffusion coefficient calculated from MSD curves between *in situ* TEM results and MD simulations should be attributed to the following reasons: (1) The observed droplets from *in situ* TEM was in dozens of nanometer scale. In contrast, MD simulation focused on ion-complex groups with few nanometer scale, so the diffusion and movement were intensified. (2) The thin liquid layer in electrochemical liquid cells also limited the motion rate of LiPSs droplets.

In the limit of low Reynolds number, we measured the velocity and interaction force of the droplet-like structure. For a nearly spherical droplet with a constant radius R, the interaction force F is proportional to the drag coefficient γ, and the Stokes' law gives:

$$F = \gamma v = (6\pi\eta R)v \quad \text{(Eq. S2)}$$

where η is the viscosity of electrolyte ($s\ m^{-2}$), and v is the velocity of droplet-like structure ($nm\ s^{-1}$). The mobility μ is the inverse of the drag coefficient γ. According to Einstein relation ($D = \mu k_B T/q$), diffusion coefficient is proportional to its mobility constant. The Einstein-Stokes equation can be given:

$$D = k_B T/6\pi\eta R \quad \text{(Eq. S3)}$$

where k_B is Boltzmann constant ($1.38 \times 10^{-23}\ J\ K^{-1}$), and T is temperature (300 K). Substituting in the drag coefficient γ of a nearly spherical droplet-like structure from Stokes' law, the interaction force F can be calculated:

$$F = (k_B T/D)v \quad \text{(Eq. S4)}$$

The calculated interaction force and velocity between active centers and droplet #1 was shown in Fig. 4d.

Methods of DFT calculation

In order to determine the experimentally observed Li_2S_2 crystal structure, tetragonal Li_2S_2 structure and various hexagonal Li_2S_2 structures were constructed for stability analysis. Hexagonal Li_2S_2 were constructed based on hexagonal A_2B_2 candidates, including Li_2O_2, Na_2O_2, Na_2S_2, Na_2Se_2, K_2O_2, K_2S_2, Rb_2S_2 (Extended Data Fig. 2a-d). N-doped graphene containing Mo nanoclusters with different sizes (unit cell size: 17.09 Å×17.22 Å×22 Å) was considered as the theoretical model for the calculation of monomer adsorption strength. The model contained 106 C atoms and 4 N atoms (with a 2-atom defect site for anchoring the Mo nanoclusters in Mo NCs/N-G), where the Mo nanoclusters contained 1, 4, and 9 Mo atoms, respectively. The spin-polarized DFT calculations were carried out by using Vienna Ab initio Simulation Package (VASP.5.4.4)[46]. The correlation energy and exchange energy were calculated by using the PBE form of the generalized gradient approximation[47]. The cut-off energy of plane wave was 500 eV. The number of k-points in the Brillouin zone multiplied by the lattice parameter in each dimension was approximately 20. The structural optimization was carried out at a convergence of 0.01 eV $Å^{-1}$ on the force. Additionally, the semiempirical van der Waals correction method of Grimme (DFT-D3) was used to describe the dispersion interaction[48].

The formation energy (E_f) of different Li_2S_2 structures was calculated by:

$$E_f = E_{crystal}/n \quad \text{(Eq. S5)}$$

where $E_{crystal}$ is the total energy of Li_2S_2 cell and n is the total atoms of the unit cell. The adsorption energy of monomers ($E_{ads\text{-}monomer}$) on each graphene slab was calculated by:

$$E_{ads\text{-}monomer} = E_{total} - E_{monomer} - E_{slab} \quad \text{(Eq. S6)}$$

where E_{total} is the total energy of the (Mo NCs/) N-G slab with one adsorbed monomer molecule. $E_{monomer}$ is the energy of an isolated monomer molecule, and E_{slab} is the energy of the (Mo NCs/) N-G slab.

Mo NCs/N-G model with a 4-atom Mo nanocluster was used to investigate the charge transfer between the electrodes and LiPSs (Extended Data Fig. 8g). A solution layer containing 3 Li_2S_6, 3 LiTFSI, 12 DOL and 12 DME molecules was constructed on the surface of Mo NCs/N-G electrode. As reported by Le et al.[49], the electrode potential was simulated by adding 6 Li atoms under the Mo NCs/N-G, and these Li atoms would not diffuse into the vacuum layer or solution during the simulation. All models were charge neutral and the charges of ions were provided by bader charge analysis. The electronic structure of the interface was analysed after a relaxation of 20 ps in the NVT ensemble, and after applying the electrode potential for 8 ps (Extended Data Fig. 8g). The hybrid Gaussian and plane waves method as implemented in the Quickstep module of the CP2K package[50] was employed for AIMD simulations. The PBE functional with the Grimme D3 van der Waals correction method was used to calculate the Li diffusion. The GTH pseudopotentials combined with DZVP-MOLOPT-SR-GTH basis set was utilized for all atoms[51]. In order to speed up the structure relaxation, the H atoms in the system were changed to D atoms, and the time step was set as 1 fs. Due to the large cell size, only the Γ point in Brillouin zone was used for calculations. The second-generation Car-Parinello molecular dynamics (SGCPMD)[52,53] was used for model optimization sampling, and the system temperature was set at 350 K. The

Langevin friction coefficient (γ_L) was set to 0.001 fs^{-1}, and the region friction coefficients (γ_D) of Mo and other atoms were set to 5×10^5 fs^{-1} and 2.1×10^4 fs^{-1}, respectively.

Methods and models of MD simulation

To investigate the diffusion and aggregation behaviours of Li_2S_6 in the bulk solution, random filling models were constructed with different Li_2S_6 concentrations of 2.51 wt%, 5.28 wt%, 9.68 wt%, and 17.93 wt% (Extended Data Fig. 8a and Supplementary Figs. 24 and 25). The solution was filled with 255 LiTFSI, 1020 DOL, and 1020 DME molecules. To study the interaction between Li_2S_6 molecules and various electrodes (Mo NCs/N-G and Ti), MD models of a solution layer on the electrode surface were constructed (Extended Data Fig. 8c and Supplementary Fig. 26). The Mo NCs/N-G model, which consisted of defective N-doped graphene supported nanoclusters containing 40 Mo atoms and had a box size of 98.4 Å×76.695 Å×200 Å, was constructed from the optimized unit cell shown in Supplementary Fig. 27c. The Ti model was a 6-layer Ti (001) slab of the hcp phase, possessing a lattice parameter of 2.93 Å, and was constructed with a box size similar to that of the Mo NCs/N-G model. In order to simulate different concentrations of Li_2S_6 on the electrode surfaces, 65, 125, and 255 Li_2S_6 molecules were randomly introduced into a solution composed of 255 LiTFSI, 1020 DOL, and 1020 DME. These quantities corresponded to the Li_2S_6 concentrations of 5.28 wt%, 9.68 wt%, and 17.93 wt%, respectively. To investigate the interaction mechanism between dense ion-complex phases composed of Li^+ and S_6^{2-} and various electrodes of Mo NCs/N-G and Ti (Fig. 4e and Supplementary Fig. 27a), MD models were further expanded by increasing the simulation box size to 172.2 Å x 153.39 Å x 250 Å. The models comprised of 3060 Li_2S_6 molecules in a solution consisting of 1020 LiTFSI, 4080 DOL, and 4080 DME in a layered compact state. The models were developed to simulate the high-concentration Li_2S_6-enriched region on the electrode surface.

All MD simulations were performed using the Large-scale Atomic/Molecular Massively Parallel Simulator (LAMMPS) software package[54]. Lennard-Jones 12-6 (LJ 12-6) potential and electrostatic potential were used to describe the non-bonded interactions between particles in the system:

$$U_{ij}(r_{ij}) = 4\varepsilon_{ij}\left[\left(\frac{\sigma_{ij}}{r_{ij}}\right)^{12} - \left(\frac{\sigma_{ij}}{r_{ij}}\right)^{6} + \frac{1}{4\pi\varepsilon_0}\frac{q_i q_j}{r_{ij}}\right] \text{ (Eq. S7)}$$

where the subscript ij represents the interaction between particles i and j, U_{ij} represents the potential energy generated by the interaction, r_{ij} represents the distance between the particles and q_i is the charge on atom i. The LJ interaction parameters were calculated using the Lorentz-Berthelot combining rules ($\sigma_{ij} = (\sigma_i + \sigma_j)/2$; $\varepsilon_{ij} = \sqrt{\varepsilon_i \varepsilon_j}$). Periodic boundary conditions in the x and y directions and non-periodic boundary conditions in the z direction were used in all interfacial simulations. Furthermore, the non-bonded parameters and force constants of bonds, angles and dihedrals of DME and DOL molecules were derived from OPLS-AA force field[55], while that of LiTFSI was extracted from literatures[56]. Meanwhile, we employed the force field parameters reported by Hu et al. for Li_2S_6 molecules[57]. The parameters of Mo NCs/N-G used for the LJ interaction were referred to the work of Bernardes et al. (for Mo) and Abbaspour et al. (for N and C), respectively[58,59]. As for the atomic charges of Mo NCs/N-G model, it followed the bader charge analysis of the unit cell optimized by the above DFT calculations. The LJ interaction parameters of Ti were referred to the report by David et al[60].

In all simulations, the equations of motion were integrated using a time step of 1 fs, and temperature control was achieved by coupling LiTFSI, Li_2S_6, DOL, and DME molecules to a Nosé Hoover thermostat with a time constant of 0.1 ps[60,61], respectively. All atoms of the electrode slabs were fixed throughout the simulations.

To investigate the diffusion and aggregation behaviors of Li_2S_6 molecules in the bulk solution at various concentrations, the simulation program involved a relaxation phase of 2 ns at a pressure of 1 bar in the NPT ensemble, followed by a 90 ns NVT ensemble simulation for sampling. The clusters of S atoms whose distance from each other in the solution was less than 3.5 Å were identified and counted every 10 ps to obtain the cluster size (Extended Data Fig. 8b). The five largest S_6^{2-} clusters in the simulated system were selected, and their sizes were averaged to evaluate the aggregation of S_6^{2-} ions. To investigate the interaction between the different electrode surfaces (Mo NCs/N-G and Ti) and Li_2S_6 molecules, the simulation program involved an initial relaxation phase in the NVT ensemble for 2 ns to fully optimize the randomly constructed solution layer. This was then followed by a 90 ns simulation for sampling. The number of S atoms on different electrode surfaces was counted every 10 ps within the area of z coordinate 0–15 Å (Extended Data Fig. 8d). The high-concentration interface layers were initially relaxed at 500 K for 2 ns in the canonical ensemble. Subsequently, the temperatures were gradually lowered to 300 K to continue the simulations for 40 ns over the Mo NCs/N-G (Fig. 4e) and Ti (Supplementary Fig. 27a) surfaces. To facilitate a better comparison of interfacial diffusion, relevant statistics were gathered during the subsequent 40 ns simulations at a temperature of 350 K (specifically, between 42-82 ns, Extended Data Fig. 8e). To compare the difference in S_6^{2-} migration across different electrode interfaces, we calculated the MSD of Li_2S_6 along the Z axis (Extended Data Fig. 8f):

$$\text{MSD-Z} = \langle (z\text{-}z_0)^2 \rangle = \frac{1}{N}\sum_{n=1}^{N} \left(z_n(t)\text{-}z_n(0)\right)^2 \quad \text{(Eq. S8)}$$

where N is the number of S atoms of Li_2S_6 in the simulation box, $z_n(t)$ is the z position of each S atom at time t, $z_n(0)$ is the reference z position of each S atom.

To investigate the redistribution of S_6^{2-} ions near the electrode induced by the Mo active centers, the simulation box was divided into slices of 0.5 Å thickness. The number of S_6^{2-} ions in each slice was computed every 10 ps, and the average number of S_6^{2-} ions in each slice was recorded every 1 ns to calculate the charge density of S_6^{2-} ions, as shown in Fig. 4f and Supplementary Fig. 27d:

$$\rho_Q = \frac{q_{S6} \times \sum_{z}^{z+0.5} n_{S6}}{V_{slice}} \quad \text{(Eq. S9)}$$

where q_{S6} is charge of one S_6^{2-} ion (i.e., 2), n_{S6} is the total number of S_6^{2-} ions in the slice with a thickness of 0.5 Å in the z direction and V_{slice} is the volume of the slice.

Structure characterization of Mo NCs/N-G

The nanocluster active center immobilized surface, Mo NCs/N-G nanosheet, was designed for the following considerations: high reactivity of atomically isolated metal sites, and easy integration on liquid-cell electrodes for high-resolution observation. Mo NCs/N-G was prepared by coupling the negatively charged POMs with positively charged amino groups of graphene, which ensured the monodispersed distribution and isolated anchoring of POMs (Supplementary Fig. 18). HRTEM image and XRD pattern revealed the amorphous structure of Mo NCs/N-G nanosheet (Fig. 3a and Supplementary Fig. 19a). HAADF-STEM image further confirmed the monodispersed Mo nanoclusters, with an average size of 1.1 nm and a content of 6.9 wt% (Fig. 3b and Supplementary Fig. 19b, c). In XANES, the absorption energy of Mo NCs/N-G was between MoO_2/MoO_3 and Mo foil, indicating a positively charged active center (Supplementary Fig. 19d). XPS detected three main peak regions corresponding to the valence states of Mo^0, Mo^{+4}, and Mo^{+6} (Supplementary Fig. 19e). The XANES linear combination fitting revealed that the percentage of these valence states were 10%, 57%, and 33%, respectively (Supplementary Fig. 20). FT-EXAFS showed that the strongest peak of Mo NCs/N-G was located at about 1.4 Å (Fig. 3c), which indicates that Mo atoms were mainly bonded to N atoms (Supplementary Fig. 19f).

Electrochemical performance of Li-S full cells

Electrochemical performance of Mo NCs/N-G/S with high sulfur loading (80 wt%) was investigated under high mass loading, fast charging, and lean electrolyte conditions. Mo NCs/N-G/S exhibited a cycling performance of 887 mA h g^{-1} at 1 C for 100 cycles and rate capability of 1525, 1127, 1018, 942, 879, 766, 639 mA h g^{-1} at 0.1, 0.2, 0.5, 1, 2, 3, 4 C, respectively (Extended Data Fig. 10a-c). At the increasing sulfur areal loading of 2, 3.5, 5.4 (E/S = 4.3 µL mg^{-1}_s), and 7 mg cm^{-2} (5.1 µL mg^{-1}_s), it delivered the areal capacities of 2.3, 3.9, 5.5, and 6.6 mA h cm^{-2} over 40 cycles (Extended Data Fig. 10d). At 2 and 3 C, it delivered discharge capacities of 645 and 573 mA h g^{-1} after 500 cycles with low-capacity decay of 0.038% and 0.047% per cycle (Extended Data Fig. 10e).

Data availability

The data that support the findings of this study are available from the corresponding authors upon reasonable request.

Reference

40. Müller, A. et al. Organizational Forms of Matter: An Inorganic Super Fullerene and Keplerate Based on Molybdenum Oxide. *Angew. Chem. Int. Ed.* **37**, 3360-3363 (1998).
41. Hummers, W. S. & Offeman, R. E. Preparation of Graphitic Oxide. *J. Am. Chem. Soc.* **80**, 1339 (1958).
42. Cowley, J. M. & Moodie, A. F. The scattering of electrons by atoms and crystals. I. A new theoretical approach. *Acta Cryst.* **10**, 609-619 (1957).
43. Goodman, P. & Moodie, A. F. Numerical evaluations of N-beam wave functions in electron scattering by the multi-slice method. *Acta Cryst.* **A30**, 280-290 (1974).
44. Liao, H.-G., Cui, L., Whitelam, S. & Zheng, H. Real-Time Imaging of Pt_3Fe Nanorod Growth in Solution. *Science* **336**, 1011-1014 (2012).

45. Zheng, H. *et al.* Nanocrystal Diffusion in a Liquid Thin Film Observed by in Situ Transmission Electron Microscopy. *Nano Lett.* **9**, 2460-2465 (2009).
46. Kresse, G. & Furthmüller, J. Efficiency of Ab-initio Total Energy Calculations for Metals and Semiconductors Using a Plane-Wave Basis Set. *Comput. Mater. Sci.* **6**, 15-50 (1996).
47. Perdew, J. P., Burke, K. & Ernzerhof, M. Generalized Gradient Approximation Made Simple. *Phys. Rev. Lett.* **77**, 3865-3868 (1996).
48. Grimme, S., Antony, J., Ehrlich, S. & Krieg, H. A Consistent and Accurate Ab Initio Parametrization of Density Functional Dispersion Correction (Dft-D) for the 94 Elements H-Pu. *J. Chem. Phys.* **132**, 154104 (2010).
49. Le, J.-B., Fan, Q.-Y., Li, J.-Q. & Cheng, J. Molecular origin of negative component of Helmholtz capacitance at electrified Pt(111)/water interface. *Sci. Adv.* **6**, eabb1219 (2020).
50. Hutter, J., Iannuzzi, M., Schiffmann, F. & VandeVondele, J. cp2k: atomistic simulations of condensed matter systems. *WIREs Comput. Mol. Sci.* **4**, 15-25 (2014).
51. Jain, A. *et al.* Commentary: The Materials Project: A materials genome approach to accelerating materials innovation. *APL Mater.* **1**, 011002 (2013).
52. Kühne, T. D., Krack, M., Mohamed, F. R. & Parrinello, M. Efficient and Accurate Car-Parrinello-like Approach to Born-Oppenheimer Molecular Dynamics. *Phys. Rev. Lett.* **98**, 066401 (2007).
53. Lan, J., Hutter, J. & Iannuzzi, M. First-Principles Simulations of an Aqueous CO/Pt(111) Interface. *J. Phys. Chem. C* **122**, 24068-24076 (2018).
54. Dodda, L. S., Vaca, I. C. d., Tirado-Rives, J. & Jorgensen, W. L. Fast Parallel Algorithms for Short-Range Molecular Dynamics. *J. Comput. Phys.* **117**, 1-19 (1995).
55. Dodda, L. S., Cabeza de Vaca, I., Tirado-Rives, J. & Jorgensen, W. L. LigParGen web server: an automatic OPLS-AA parameter generator for organic ligands. *Nucleic Acids Res.* **45**, W331-W336 (2017).
56. Zhang, Y. *et al.* Water-in-Salt LiTFSI Aqueous Electrolytes. 1. Liquid Structure from Combined Molecular Dynamics Simulation and Experimental Studies. *J. Phys. Chem. B* **125**, 4501-4513 (2021).
57. Hu, T. *et al.* Understanding Structural and Transport Properties of Dissolved Li_2S_8 in Ionic Liquid Electrolytes through Molecular Dynamics Simulations. *Chemphyschem* **22**, 419-429 (2021).
58. Abbaspour, M., Akbarzadeh, H. & Zaeifi, S. Thermodynamics, Structure, and Dynamic Properties of Nanostructured Water Confined into B-, N-, and Si-Doped Graphene Surfaces and Carbon Nanotubes. *Ind. Eng. Chem. Res.* **59**, 9642-9654 (2020).
59. Bernardes, C. E., Canongia Lopes, J. N. & Minas da Piedade, M. E. All-atom force field for molecular dynamics simulations on organotransition metal solids and liquids. Application to $M(CO)_n$ (M = Cr, Fe, Ni, Mo, Ru, or W) compounds. *J. Phys. Chem. A* **117**, 11107-11113 (2013).
60. Hoover, W. G. Canonical dynamics: Equilibrium phase-space distributions. *Phys. Rev. A* **31**, 1695-1697 (1985).
61. Nosé, S. A molecular dynamics method for simulations in the canonical ensemble. *Mol. Phys.* **52**, 255-268 (2006).

Acknowledgements This work was supported by the National Natural Science Foundation of China (Grants no. U22A20396, 22288102, 32101217, 22021001, 21991151, 21991150, and 91934303) and Fundamental Research Funds for the Central Universities (20720220009). Research at the Argonne National Laboratory was funded by the US Department of Energy (DOE), Vehicle Technologies Office. Support from Tien Duong of the US DOE's Office of Vehicle Technologies Program is gratefully acknowledged. Use of the Advanced Photon Source (APS), an Office of Science user facilities, was supported by the US Department of Energy, Office of Science and Office of Basic Energy Sciences, under contract no. DE-AC02-06CH11357. G. X. and K. A. also thank the support from Clean Vehicles, US-China Clean Energy Research Center (CERC-CVC2). S. Z. thanks the support from Xiamen University Nanqiang Cultivation Program for Outstanding Doctoral Students.

We sincerely thank Dr. Y. Cheng and Pro. M.-S. Wang (College of Materials, Xiamen University), Dr. Sha Li and Dr. Chen-Guang Shi (College of Chemistry and Chemical Engineering, Xiamen University) for helpful discussion and suggestion on *in situ* TEM, Raman, and XRD characterizations.

Author contributions S.-G. S., H.-G. L., G.-L. X. and K. A. conceived and supervised this work. S. Z. designed the experiments, conducted TEM, materials synthesis, electrochemistry, and wrote the paper. J. S. conducted the DFT calculations and MD simulations. J.-F. C., Y. Q., Y. L. and L. H. participated in discussions and data analysis. S. L., G. L. and Y. C. analysed the TEM characterization. F. P. and Q. Z. measured the electrochemical performance. C. Z., I. H., and C.-J. S. conducted XAS characterization. J. D. fabricated electrochemical liquid cells. J. L. and Y. D. conducted EELS characterization. All authors participated in the analysis of experimental data and discussion of the results, as well as in writing and revision of the manuscript.

Competing interests The authors declare no competing interests.

Additional information

Correspondence and requests for materials should be addressed to Hong-Gang Liao, Gui-Liang Xu, or Khalil Amine.

Reprints and permissions information is available at http://www.nature.com/reprints.

Extended Data Legends

Extended Data Fig. 1 | Configuration of the liquid-cell EC-TEM. (a) Schematic illustration of an electrochemical liquid cell from top and side views, composed of top/bottom chips with 10 nm SiN_x observation windows, 100 nm spacers, and samples on electrodes. (b) Digital photographs of EC-TEM holder and electrochemical liquid cell. (c, d) Schematic process of liquid-cell preparation in an argon-filled glovebox. After liquid-cell assembly, the pre-prepared Li_2S_6 electrolyte with various concentrations was injected and filled by capillary force, before sealed with epoxy. (e) HRTEM image and corresponding FFT pattern of Li_2S@graphene loaded on a single bottom chip with 11.2 nm SiN_x layers. The thickness of the SiN_x layers was measured using a spectroscopic ellipsometer with a spectral range of 193–1000 nm. (f) Time-series HRTEM images of Li_2S@graphene (red frame) showing the high-spatial resolution and stable atomic structure at a dose rate of 18200 e $Å^{-2}$ s^{-1}.

Extended Data Fig. 2 | Crystal structure of the simulated Li_2S_2. (a) The fixed lattice parameters of tetragonal Li_2S_2 and hexagonal Li_2S_2 simulated based on multiple hexagonal A_2B_2 structures. (b) The corresponding energy comparison between tetragonal Li_2S_2 and hexagonal Li_2S_2. The hexagonal Li_2S_2 structures were constructed based on Li_2O_2, Na_2O_2, Na_2S_2, Na_2Se_2, K_2O_2, K_2S_2, Rb_2S_2, arranged from left to right in the blue frame. (c) The simulated crystal structures of hexagonal Li_2S_2 with P63/mmc and $P\bar{6}2m$ space groups. (d) The crystal structures and simulated electron diffraction of tetragonal Li_2S_2 along [001] and [111] directions, respectively. The abnormal systematic extinction of electron diffraction in Fig. 2d, that was, the appearance of (100) and (300), should be attributed to the lattice defect of Li_2S_2, which led to the diffraction deviating from Bragg condition, and the secondary diffraction occurred. (e) SAED pattern of granular Li_2S_2 (tetragonal, $P4_2$/mnm) along [111] direction. (f) SAED patterns of rod-like Li_2S (cubic, Fm-3m) along [100] and [011] directions. (g) Elemental weight ratio according to EDS spectrum in Fig. 2f. The red and blue balls represent Li and S atoms, respectively.

Extended Data Fig. 3 | Interfacial reactions of LiPSs at –0.1 V without mediation of active centers. (a) Comparison of output current during potentiostatic discharge at –0.1 and –0.5 V in electrochemical liquid cells. The current density was reduced by half at –0.1 V. (b) The projection area variation as a function of time of particles #5 and #6. Error bars represent standard deviations of the measurement. (c) Time-series TEM images from Supplementary Video 3 showing two-step Li_2S deposition in an electrochemical liquid cell during potentiostatic discharge at –0.1 V. 10 mM Li_2S_6 was used as the electrolyte. (d) Statistics of rod and particle quantity at specific times corresponding to the white frame areas in the TEM image (0.6 s). (e) Time-series TEM images of typical two-step deposition of Li_2S via metastable Li_2S_2 (marked by white dotted lines). TEM images of I-IV correspond to the typical areas at 72.6 s.

Extended Data Fig. 4 | *In situ* EC-TEM studies of Li_2S deposition with mediation of active centers. (a) The projection area variation as a function of time of Mo NCs/N-G and time-series TEM images from Supplementary Video 4. The electrochemical liquid cell was potentiostatically discharged at –0.5 V using 10 mM Li_2S_6 as the electrolyte. Error bars represent standard deviations of the measurement. (b) Time-series TEM images to further observe the red-square area of Extended Data Fig. 4a (185s) under a higher magnification (Supplementary Video 5). The electrochemical liquid cell was further potentiostatically discharged at –0.5 V. Many dark areas (marked with red circles) and deposited particles (marked with white arrows) were observed. (c) Time-series TEM images from Supplementary Video 6. The electrochemical liquid cell was potentiostatically discharged at –0.5 V using 100 mM Li_2S_6 as electrolyte. The imaging area was divided into electron inaccessible/accessible areas. Li_2S deposition mainly proceeded on electron accessible areas of Mo NCs/N-G, while no change was observed on electron inaccessible area and bare Ti electrode surface. This indicated the high reaction activity of Mo NCs/N-G for electrochemical deposition of Li_2S.

Extended Data Fig. 5 | Method of HRTEM observation in an electrochemical liquid cell. (a) Schematic illustration of "e-beam bubble generation" method for HRTEM observation of Li_2S nanocrystalline deposited on Mo NCs/N-G nanosheet. Following the electrochemical deposition of Li_2S through a potentiostatic discharge at –0.5 V, the e-beam was focused on the bulk electrolyte for the generation of bubble. Once the bubble area stabilized, the atomic structure of Li_2S nanocrystalline can be obtained, with the image resolution being mainly determined by the thickness of SiN_x layers. (b) TEM images showing different areas of the LiPSs electrolyte, Li_2S nanocrystalline deposited on Mo NCs/N-G, and the stabilized bubble area. (c, d) HRTEM images before and after the removal of the wetting layer of electrolyte. (e, f) Annular dark field scanning TEM (ADF-STEM) image and the corresponding EELS image for relative thickness measurement in liquid cells. (g) Typical low-loss EELS of Li_2S nanocrystalline (I), Mo NC/N-G nanosheets (II), and SiN_x layers (III) as marked in the EELS image. (h) Average relative thickness obtained by the log-ratio method in Digital Micrograph software. Error bars represent standard deviations from multiple EELS curves. (i) Time-series HRTEM images, corresponding FFT patterns, and partial enlarged details of Li_2S nanocrystalline deposited on Mo NCs/N-G obtained in an electrochemical liquid cell.

Extended Data Fig. 6 | Analysis of *in situ* EC-TEM studies of LiPSs redox reactions with mediation of active centers. (a) Time-series TEM images from Supplementary Video 7 showing multiple droplets in different areas (highlighted in red). (b) Motion trajectory of the mass center of droplet #1 and the corresponding edge contour plots of droplet #1 in Fig. 4b. It included the typical processes of gathering, conversion, and crystallization. (c) Projection area variation of droplets #2 and #3 (red), and Mo NCs/N-G (blue) as a function of time during potentiostatic discharge. A power function was used to fit the area variation of droplets #2 and #3 over time (Area ∝ t^n)

according to LSW model, where n≥1 represents reaction-limited growth. After a rapid decrease in the size of LiPSs droplets, there was an obvious increase in the projection area of Mo NCs/N-G nanosheet, similar to that in Extended Data Fig. 4a, b, which should be attributed to the deposition of Li_2S. Error bars represent standard deviations of the measurement. (d) MSD analysis of droplet #1 as a function of time. The two-dimensional diffusion coefficient (D) was calculated to be 4.71 $nm^2\ s^{-1}$. The initial point of MSD corresponds to 34.4 s of droplet #1 in Fig. 4b.

Extended Data Fig. 7 | Structure characterization of droplet-like dense phase. (a, b) Comparative characterization of LiPSs dense phase and Li_2S nanocrystalline, including HRTEM images, the corresponding FFT and SAED patterns, HAADF-STEM images, EDS mappings, and the corresponding linear elemental analysis. (c) TEM and HAADF-STEM images of Mo NCs/N-G nanosheet after the electrochemical deposition in a liquid cell, showing the LiPSs dense phase and Li_2S nanocrystalline from a wider observation region. (d) Raw and post-processed HRTEM images using a Gaussian filter. To solve the scattering and artifacts in HRTEM images resulting from amorphous SiN_x windows, disordered electrolyte, and the contrast transfer function of the electron microscope, a Gaussian filter was applied to suppress high-spatial frequency noise and enhance the boundary of dense phase areas. (e, f) Partial enlarged details of HAADF-STEM image and the corresponding linear HAADF intensity analysis. The areas of LiPSs dense phase were marked by the white dotted lines. The linear HAADF intensity analysis was marked by the white arrow. The contrast contribution of HAADF intensity can be attributed to Li_2S nanocrystalline, LiPSs dense phase, electrolyte, and background, respectively. (g) Schematic illustration of the path of scattered electrons.

Extended Data Fig. 8 | MD simulations and DFT calculations at different interfaces. (a) Snapshots of MD simulations with different Li_2S_6 concentrations of 5.28 wt% and 17.93 wt%. (b) Statistics of S atoms in aggregated clusters with different electrolyte concentration. The five largest clusters were used to calculate the average number of contained S atoms. (c) Snapshots of MD simulations on different surfaces of Mo NCs/N-G and Ti with Li_2S_6 concentration of 5.28 wt%. The right row was the enlarged view of the interface details, and the initial S_6^{2-} and Li^+ ions were randomly dispersed in the electrolyte. After the NVT relaxation of 2 ns, the sampling results indicated that Mo NCs/N-G had a strong long-range attraction with S_6^{2-} ions. (d) Statistics of S atoms attracted to the electrode surfaces of Mo NCs/N-G and Ti with different electrolyte concentration. (e) Comparison of Z-axis position variation (Å) of dense ion-complex phase at different interfaces as a function of time corresponding to MD simulations in Fig. 4e with Li_2S_6 concentration of 17.93 wt%. The Z-axis distance is defined from LiPSs droplet to the electrode surfaces (Ti or Mo NCs/N-G). (f) MSD analysis of Li_2S_6 movement along the Z-axis direction. The diffusion coefficients of S atoms in Li_2S_6 molecules over Mo NCs/N-G (D_1) and Ti (D_2) surfaces were 2.73×10^{-7} $cm^2\ s^{-1}$ and 4.88×10^{-9} $cm^2\ s^{-1}$, respectively. The initial point of MSD corresponds to 42 ns of the simulation. (g) AIMD simulation of charge variation of polysulfide ions around Mo active centers from a top view and a side view. Considering the dynamic charge distribution, the polysulfide ions in the dense phase are defined as S_6 ions in AIMD simulations. S_6 ions in the dense phase are divided into internal, middle, and external layers according to the distances from Mo active centers when viewed from the top. The charge distribution diagrams, shown from left to right, include (I) pristine structure relaxed for 20 ps before applying the electrode potential, simulations at (II) 0 ps and (III) 8 ps after applying the electrode potential.

Extended Data Fig. 9 | Evaluation of electrochemical behaviour using Li_2S_6 electrolyte (100 mM) in coin-type cells. (a) Potentiostatic discharge profiles of Li_2S deposition at 2.05 V with/without active centers. The scale of y-axis is indicated by the bar. (b) Nyquist profiles of EIS after potentiostatic discharge. R_e, R_s, and R_{ct} indicate the resistance of electrolyte, surface layer, and charge transfer, respectively. The inset is the local magnification profiles. (c) Potentiostatic charge profiles of Li_2S dissolution at 2.4 V with/without active centers. The scale of y-axis is indicated by the bar. (d) Arrhenius plots of the linear relationship between logarithmic values of the reciprocal of R_{ct} and the reciprocal of absolute temperatures for 1.7, 1.8, 1.9, and 2.0 V, with (red)/without (blue) active centers. (e) Comparison of the corresponding E_a calculated based on the slope of linear fitting. The E_a values with/without active centers were 0.27/0.5, 0.23/0.5, 0.17/0.49, and 0.19/0.49 eV, corresponding to the discharge potentials of 2.0, 1.9, 1.8, and 1.7 V, respectively. (f) CV profiles of symmetric cells with/without active centers at a scan rate of 0.1 mV s^{-1}. (g) Comparison of cycling performance with/without mediation of active centers at 16 μA cm^{-2}. (h, i) Corresponding charge/discharge profiles at specific cycles, showing the energy barriers of Li_2S nucleation and dissolution.

Extended Data Fig. 10 | Evaluation of electrochemical performance in Li-S batteries. (a, b) Cycling performance (1 C, 100 cycles) and rate performance (0.2, 0.5, 1, 2, 3, 4, and 0.2 C) of Mo NCs/N-G/S, with the sulfur areal loading of 2 mg cm^{-2}. A battery activation was performed at 0.2 C for 2 cycles (cycling performance) and 0.1 C for 1 cycle (rate performance), respectively. (c) Charge/discharge profiles from rate performance of Mo NCs/N-G/S at 0.2, 0.5, 1, 2, 3, and 4 C, respectively. (d) Cycling performance of Mo NCs/N-G/S at 0.2 C for 40 cycles with different sulfur areal loading of 2, 3.5, 5.4, and 7 mg cm^{-2}. A battery activation was performed at 0.05 C for 2 cycles. (e) Long-term and high-rate cycling performance at 2 and 3 C for 500 cycles. A battery activation was performed at 0.2 C for 2 cycles. The capacity value is selected every five cycles.

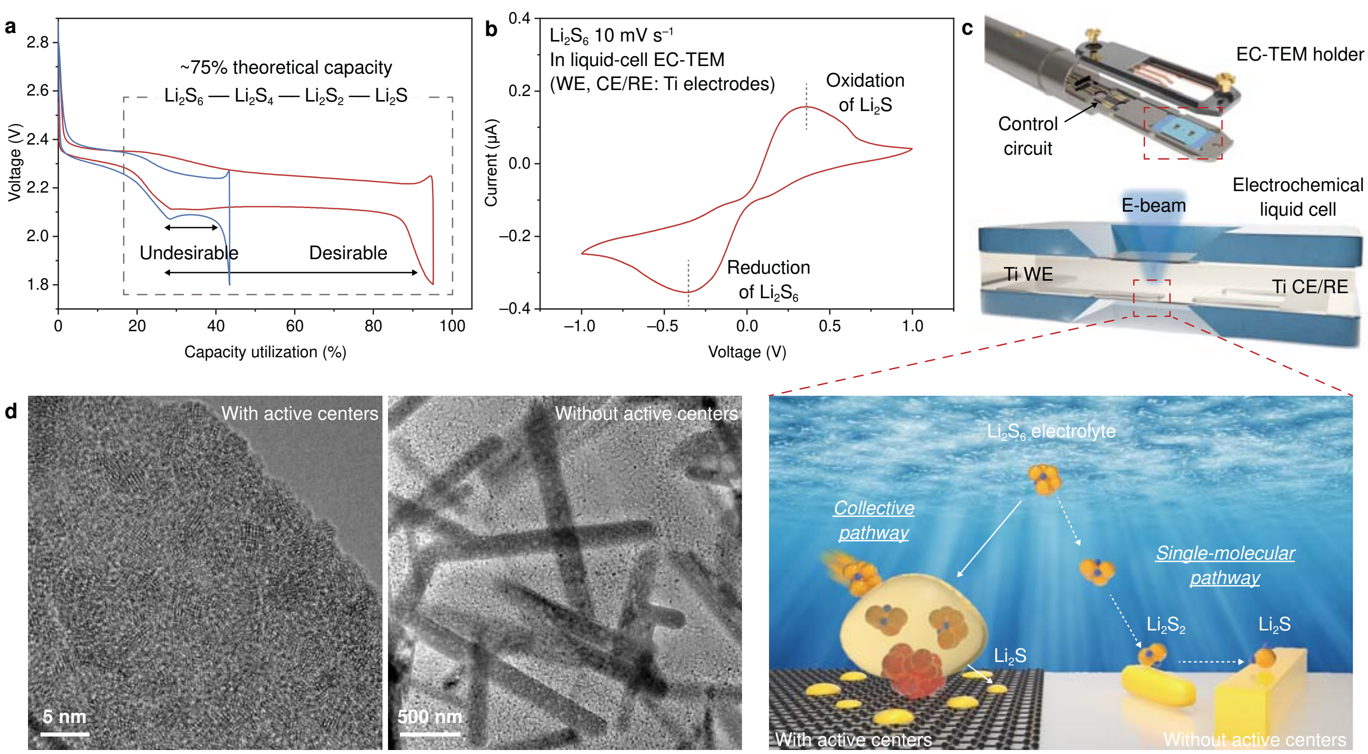

a
~75% theoretical capacity
Li2S6 — Li2S4 — Li2S2 — Li2S
Undesirable
Desirable
Voltage (V)
Capacity utilization (%)
b
Li2S6 10 mV s−1
In liquid-cell EC-TEM
(WE, CE/RE: Ti electrodes)
Oxidation of Li2S
Reduction of Li2S6
Current (μA)
Voltage (V)
c
EC-TEM holder
Control circuit
Electrochemical liquid cell
E-beam
Ti WE
Ti CE/RE
d
With active centers
Without active centers
5 nm
500 nm
Li2S6 electrolyte
Collective pathway
Single-molecular pathway
Li2S2
Li2S
With active centers
Without active centers

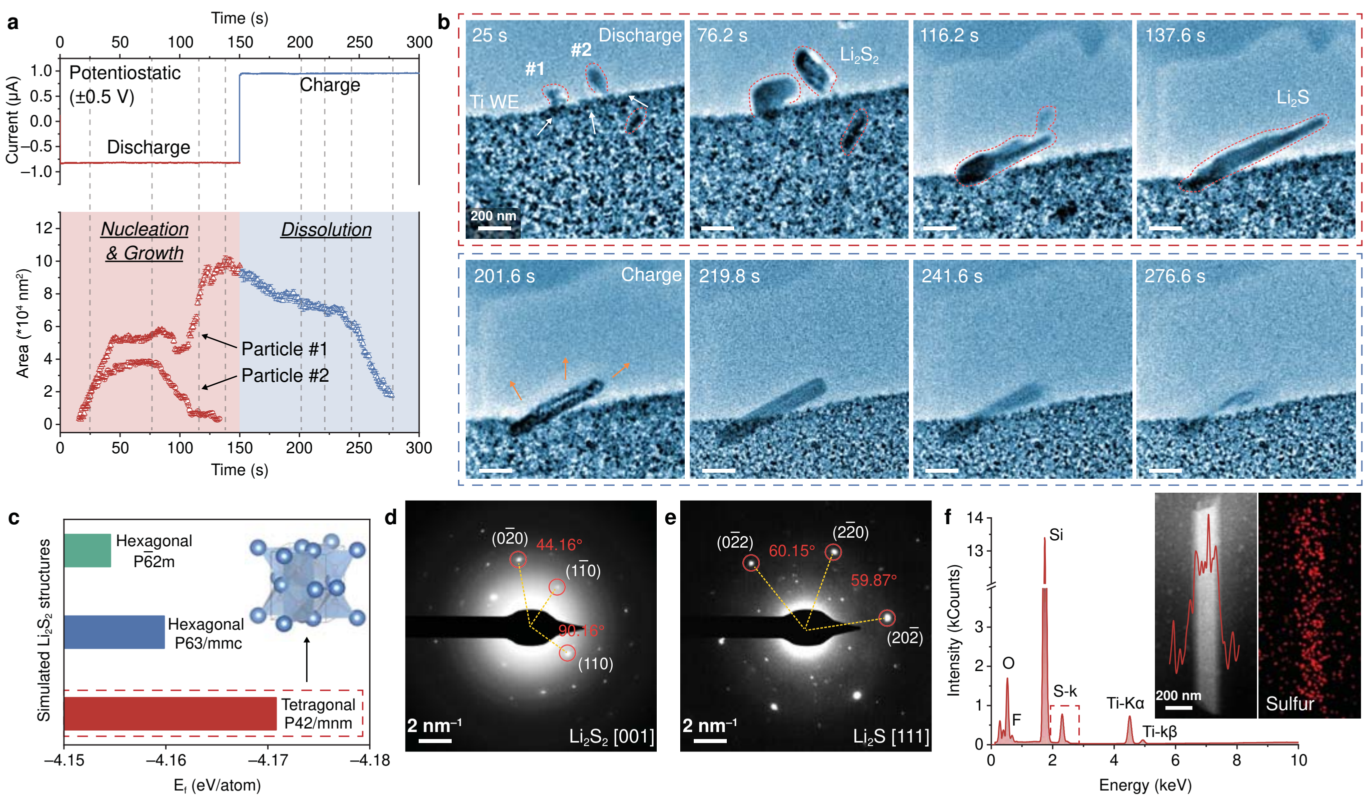

a
Time (s)
Potentiostatic (±0.5 V)
Charge
Discharge
Current (μA)
Nucleation & Growth
Dissolution
Area (*10⁴ nm²)
Particle #1
Particle #2
Time (s)
b
25 s
Discharge
#1
#2
Ti WE
200 nm
76.2 s
Li2S2
116.2 s
137.6 s
Li2S
201.6 s
Charge
219.8 s
241.6 s
276.6 s
c
Hexagonal P-62m
Hexagonal P63/mmc
Tetragonal P42/mnm
Simulated Li2S2 structures
Ef (eV/atom)
d
(0-20)
44.16°
(1-10)
90.16°
(110)
2 nm⁻¹
Li2S2 [001]
e
(0-2-2)
60.15°
(2-20)
59.87°
(20-2)
2 nm⁻¹
Li2S [111]
f
Si
O
F
S-k
Ti-Kα
Ti-kβ
Intensity (kCounts)
Energy (keV)
200 nm
Sulfur

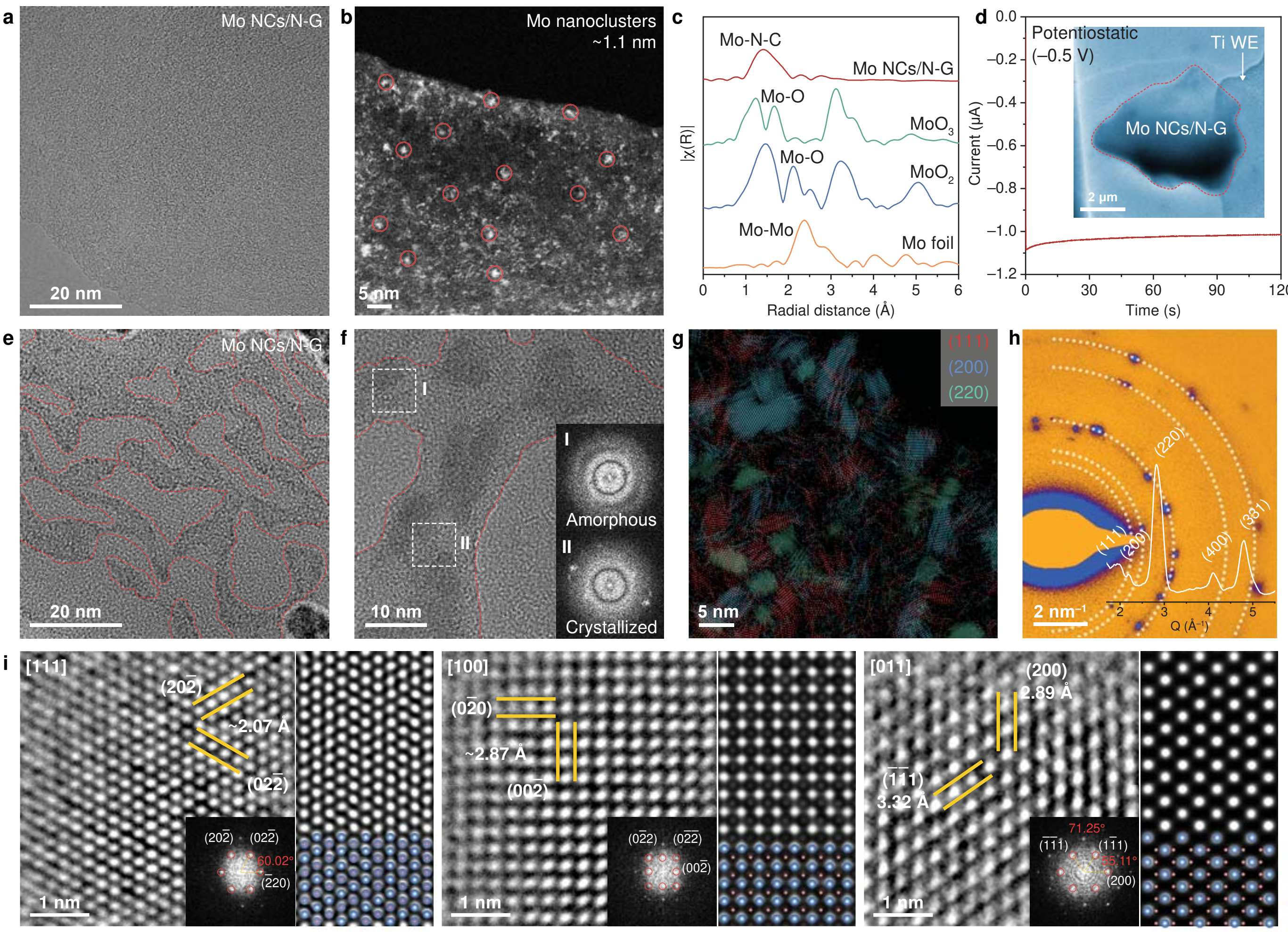

a
Mo NCs/N-G
20 nm
b
Mo nanoclusters
~1.1 nm
5 nm
c
Mo-N-C
Mo NCs/N-G
Mo-O
MoO3
Mo-O
MoO2
Mo-Mo
Mo foil
|χ(R)|
Radial distance (Å)
d
Potentiostatic
(−0.5 V)
Ti WE
Mo NCs/N-G
2 μm
Current (μA)
Time (s)
e
Mo NCs/N-G
20 nm
f
I
II
Amorphous
Crystallized
10 nm
g
(111)
(200)
(220)
5 nm
h
(111)
(200)
(220)
(400)
(331)
2 nm−1
Q (Å−1)
i
[111]
(20$\bar{2}$)
~2.07 Å
(02$\bar{2}$)
60.02°
(220)
1 nm
[100]
(0$\bar{2}$0)
~2.87 Å
(00$\bar{2}$)
(0$\bar{2}$2)
(0$\bar{2}\bar{2}$)
(002)
1 nm
[011]
(200)
2.89 Å
($\bar{1}\bar{1}$1)
3.32 Å
71.25°
55.11°
(1$\bar{1}$1)
1 nm

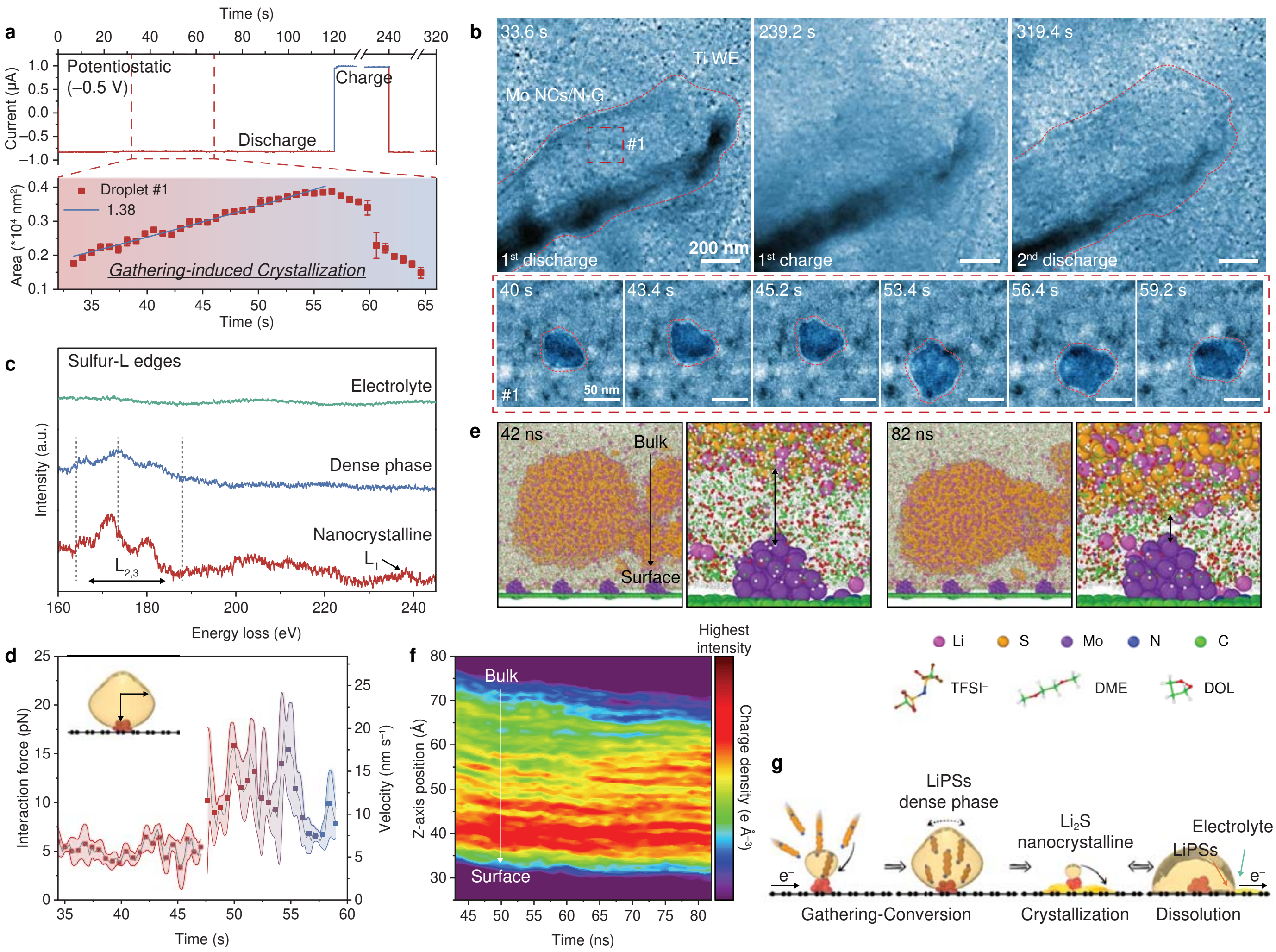
a
Time (s)
Potentiostatic (−0.5 V)
Charge
Discharge
Current (μA)
Droplet #1
1.38
Gathering-induced Crystallization
Area (*10⁴ nm²)
Time (s)
b
33.6 s
239.2 s
319.4 s
Ti WE
Mo NCs/N-G
#1
200 nm
1st discharge
1st charge
2nd discharge
40 s
43.4 s
45.2 s
53.4 s
56.4 s
59.2 s
50 nm
c
Sulfur-L edges
Electrolyte
Dense phase
Nanocrystalline
L2,3
L1
Intensity (a.u.)
Energy loss (eV)
d
Interaction force (pN)
Velocity (nm s⁻¹)
Time (s)
e
42 ns
82 ns
Bulk
Surface
Li
S
Mo
N
C
TFSI⁻
DME
DOL
f
Highest intensity
Bulk
Surface
Z-axis position (Å)
Charge density (e Å⁻³)
Time (ns)
g
LiPSs dense phase
Li2S nanocrystalline
Electrolyte
LiPSs
e⁻
Gathering-Conversion
Crystallization
Dissolution